ADVANCED OPTICAL MATERIALS
www.advopticalmat.de

High-Accuracy and Broadband Wavelength Sensor with Detection Region Ranging from Deep Ultraviolet to Near Infrared Light

*Chun-Yan Li, Yu-Tian Xiao, Can Fu, Feng-Xia Liang, Li-Miao Chen, Di Wu, and Lin-Bao Luo**

In this paper, a broadband wavelength sensor which is composed of two horizontally stacked photodetectors is reported. The top part is a monolayer graphene (MLG)/thin Si/MLG heterojunction device and the bottom part is a MLG/Ge Schottky junction device. Owing to the thin thickness of the Si and the wavelength-dependent absorption coefficients of both Si and Ge, the two photodetectors exhibit sharp contrast in photon-generation rate when illuminated with different wavelengths of light. This distinction in photon generation leads to completely different evolution in photocurrent, and the corresponding relationship between the photocurrent ratio and wavelength can be easily expressed as a monotonic function, via which the wavelength in a broad range from deep ultraviolet (265 nm) to near infrared light (1550 nm) can be easily calculated. Notably, the average relative error and the average absolute error of the wavelength sensor are estimated to be 2.1% and 2.3 nm, respectively, which are much better than previously reported values.

1. Introduction

Wavelength sensor that can quantitatively detect the wavelength of light plays an important role in various fields such as image sensing, spectral analysis, optical communication, environmental monitoring, medical testing, and so on.[1–5] For example, in the field of environmental monitoring, a piece of glass fiber filter paper containing monocyandiamide was placed directly above the red–green–blue (RGB) color sensor and chip light emitting diode (LED). By monitoring the RGB color change of the light reflected from the paper, hydrogen cyanide gas can be easily detected, which is vitally important to security check.[6] In addition, according to the tri-receptor theory of human color vision, color perception in the human visual system can be predicted by using the color matching curve. Based on this, a high-resolution digital still camera was constructed using a color filter array (CFA) equipped with a charge-coupled device (CCD) to process the recognized objects and reconstruct the color images.[7]

Generally, the representative wavelength sensor has been achieved by using a broadband inorganic semiconductor photodiode combined with a dichromatic prism or a set of filters.[8,9] For example, full-color sensing can be easily achieved by employing filter arrays that consist of a periodic arrangement of red, green, and blue filters.[10] This type of sensor is characterized by relatively narrow operation range (e.g., visible light).[11] As an important complement to above filter-assisted wavelength sensors, filterless sensor has lately received increasing research interest as well.[12–14] Although this device can quantitatively discriminate the wavelength of incident light, they are however characterized by relatively narrow sensing range and complicated device structures which entail very sophisticated instrument during device fabrication process.[15–20] Thereby, high-resolution wavelength sensor with simple device geometry is in great demand.

Various study have shown that photodetectors composed of artificial nanostructures in the form of nanofilm or nanowires can exhibit unique optoelectronic characteristics.[21,22] For example, Xu et al. has recently reported that graphene/thin Si (200 nm) heterojunction can display pronounced photoresponse to UV light illumination (365 nm), but is virtually

C.-Y. Li, C. Fu, L.-B. Luo
School of Microelectronics
Hefei University of Technology
Hefei 230009, China
E-mail: luolb@hfut.edu.cn

Y.-T. Xiao
School of Physics
Hefei University of Technology
Hefei 230009, China

F.-X. Liang
School of Materials Science and Engineering and Anhui Provincial Key Laboratory of Advanced Functional Materials and Devices
Hefei University of Technology
Hefei 230009, China

L.-M. Chen
Hunan Provincial Key Laboratory of Micro & Nano Materials Interface Science
College of Chemistry and Chemical Engineering
Central South University
Changsha 410083, China

D. Wu
School of Physics and Microelectronics
Zhengzhou University
Zhengzhou 450052, China

The ORCID identification number(s) for the author(s) of this article can be found under https://doi.org/10.1002/adom.202101735.

DOI: 10.1002/adom.202101735

blind to both visible and near infrared light (NIR) illumination (from 500 to 1200 nm).[23] This unique phenomenon is associated with the relatively strong absorption in the UV region, which is reasonable considering the wavelength dependent absorption coefficient and the relatively small thickness of the Si film. What is more, many filterless wavelength sensors are composed of integrated deep and shallow *p–n* junctions on silicon. As the *p–n* junctions at different depths can discriminate different wavelengths of light, the filterless sensor can distinguish the wavelength of light in the range of 400–950 nm, with a resolution of 20 nm.[24]

Inspired by the above work, we herein report a wavelength sensor consisting of two different kinds of photodetectors: one is monolayer graphene (MLG)/thin Si/MLG heterojunction photodetector, and the other one is MLG/Ge Schottky junction photodetector. Thanks to the high transparency and exceptionally high carrier mobility, the graphene not only allows the penetration of incident light to semiconductor, but also collect the carriers during wavelength sensing process. According to technology computer aided design (TCAD) simulation, the photon-generation rate of the two photodetectors is different under various wavelengths of radiation, leading to a completely different spectral response. The relationship between the photocurrent ratio and the wavelength follows a typical monotonic function through which the wavelength of the incident light can be determined. Further device analysis finds that wavelength sensor can quantitatively detect the wavelength of incident monochromatic light in a broad range from 265 to 1550 nm, with an average relative error and average absolute error of 2.1% and 2.3 nm, respectively, which are very competitive in comparison with other wavelength sensors previously reported. We believe that the present wavelength sensor may find potential applications in some future optoelectronic systems.

2. Results and Discussion

In this study, the broadband wavelength sensor is composed of one MLG/thin Si/MLG heterojunction photodetector (PD1) and one MLG/Ge Schottky junction photodetector (PD2), which are assembled in a horizontally stacked manner (**Figure 1**a). The MLG was grown by a chemical vapor deposition (CVD) method, and the synthetic details and the fabrication of the two PDs are provided in the Experimental Section. Figure S1a, Supporting Information, shows the field emission scanning electron microscopy (FESEM) image of the thin Si-based MSM PD (Figure 1b), the interdigital metal electrodes are 0.4 cm long and 400 µm wide. What is more, the PD2 was fabricated by directly transferring MLG onto a 200 µm thick *n*-type Ge wafer with a predefined window of 3.9 mm^2 (Figure S1b, Supporting Information). From the Raman study shown in Figure S2, Supporting Information, one can see a weak D band and two strong bands due to G and 2D band, respectively, with a ratio of I_{2D}/I_G of 2.9, suggesting that the graphene is of monolayer with negligible defects.[25,26] Moreover, the sheet resistance of the MLG is estimated to be about 280 Ohm sq^{-1}, which is close to previously reported value of 260 Ohm sq^{-1}.[27] From the absorption spectra shown in

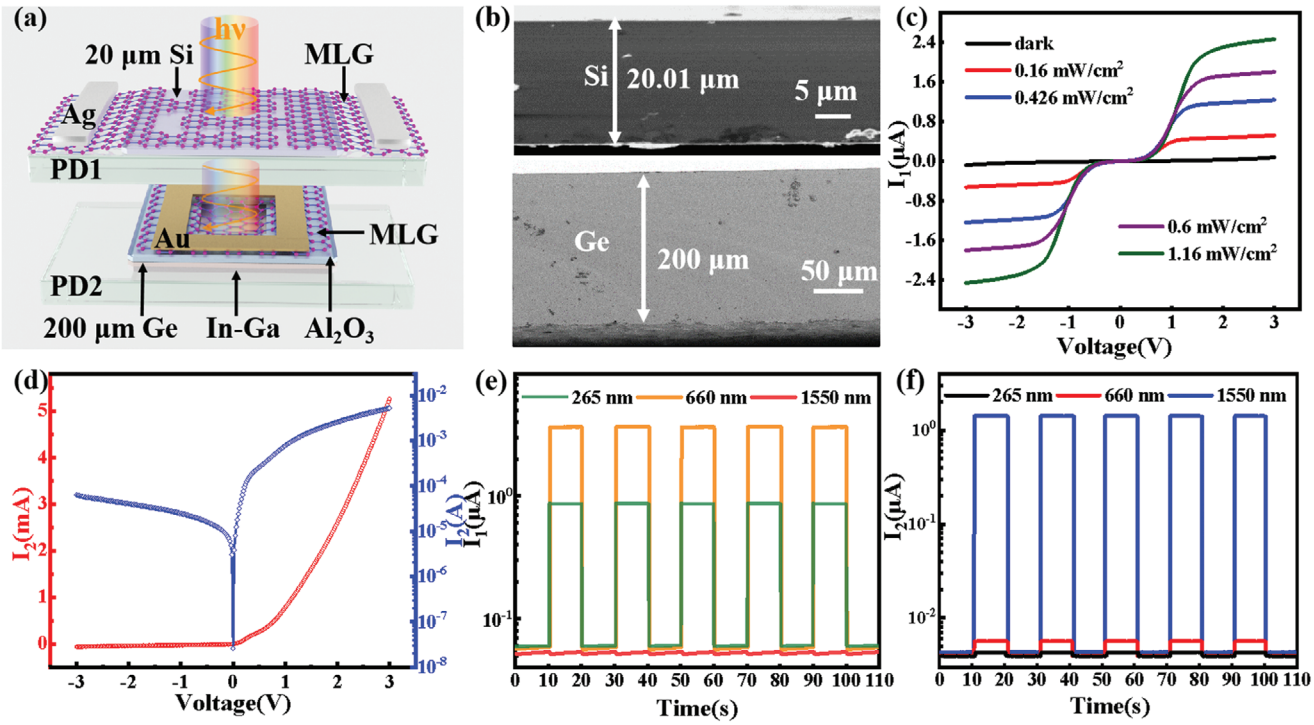

Figure 1. a) Schematic diagram of the wavelength sensor. b) Cross-sectional FESEM image of Si wafer and Ge wafer. c) *I–V* characteristics of PD1 under dark and illumination with 660 nm light with different power intensities. d) *I–V* characteristics of PD2 in linear and logarithmic coordinates, respectively, in the dark. e) Photoresponse of the PD1 under different light with an intensity of 1.2 mW cm^{-2} at 2 V. f) Photoresponse of PD2 under different light illumination with an intensity of 1.2 mW cm^{-2} at 0 V.

Figure S3, Supporting Information, it can be seen that the MLG only absorbs about 2–7% of the light in the range from UV to NIR.[28,29] This means it not only allows the majority of the incident light to reach the MLG/semiconductor interface, but also facilitates the incident light to pass through the first PD, as long as the semiconductor is thin enough. From the *I–V* shown in Figure S4a, Supporting Information, one can see that the current through PD1 is symmetric and relatively small at low bias voltage which is similar to what was observed on the metal–semiconductor–metal (M–S–M) structures.[30,31] When shined by 660 nm light illumination, the current will increase with increasing intensity (Figure 1c). Figure 1d shows the *I–V* curves of the MLG/Ge heterojunction in dark, from which the typical rectifying behavior can be observed. According to Figure S4b, Supporting Information, the PD2 exhibits a photovoltaic behavior with an open-circuit voltage (V_{OC}) of 0.028 V and a short-circuit current (I_{SC}) of 10.9 µA under 1550 nm illumination, suggesting that the PD2 is a self-driven device.[32] Figure S5, Supporting Information, confirms that the Ag and graphene, Au and graphene, and In-Ga alloy and Ge are all ohmic contacts. Figure 1e,f compares the photoresponse of PD1 and PD2 under DUV (265 nm), visible (660 nm), and NIR (1550 nm) illumination, respectively. It is noted that while both PDs show reproducible photoresponse to various light illumination, their spectral response is completely different. For example, a large photocurrent of 3.4 µA is achieved for PD1 under 660 nm light illumination with intensity of 1.2 mW cm^{-2} (Figure 1e). However, the photocurrent will decrease to 0.8 µA and 132 pA when the wavelength is switched to 265 and 1550 nm, respectively. On the contrary, the PD2 exhibits peak photoresponse in the NIR region, with a high photocurrent of 1.4 µA. Such a distinction in spectral selectivity can be ascribed to their difference in optical absorption, as shown in Figure S3, Supporting Information.

The above discrepancy in photoresponse can be understood by the schematic illustration shown in **Figure 2**. Basically, both PDs can be divided into two different regions: the depletion region and diffusion region[33] (the widths of depletion region for PD1 and PD2 are 2 and 3 µm, respectively; and the carrier diffusion lengths are 410 µm and 0.7 cm, respectively, please see Supporting Information). On the other hand, the penetration depth that denotes the transmitted distance of incident light when its intensity declines to 1/e of the initial value in semiconductor is highly dependent on the wavelength: take silicon for example, the penetration depth is only 5 nm for wavelength of 265 nm (Figure S6, Supporting Information). Nonetheless, the penetration depth will be as long as 3.9 and 156.2 µm for wavelength of 660 and 1000 nm, respectively. Because of this, the PD1 and PD2 display different spectral photoresponse: When irradiated by 265 nm light, the majority of the photons will be absorbed by the surface of the PD1. As a result, the majority of the photo-generated electron–hole pairs (EHPs) will be separated by the depletion region in PD1, contributing to photocurrent in the circuit. Meanwhile, due to the shadow effect of PD1, the photocurrent in PD2 is very small. Such a discrepancy in photocurrent will be inconspicuous when the wavelength moves to visible region. In this case, the penetration depth begins shift to diffusion region, and the PD2 begin to absorb photons, leading to narrowed difference in the photocurrent. As the wavelength increases to NIR (e.g., 1550 nm), the photocurrent of PD1 will be much smaller than that of PD2 in that the narrow bandgap of 1.12 eV can hardly absorb any 1550 nm photons, while the MLG/Ge shows peak sensitivity to this wavelength.[34]

To verify the above theory, the distribution of photon-generation rate and photocurrent was simulated by using TCAD.[35,36] For convenience, when simulating the photon-generation rate of PD1 and PD2, grid points number of 28 000 was chosen in the profile of both PDs as a compromise between computing time and precision, and the light beam shined the sensor at an angle of 90°. **Figure 3**a shows the simulated photon-generation rate of both PDs for various wavelengths (the gray part denotes glass). It can be seen that with the increase of wavelength, the area with relatively high photon-generation rate in PD1 gradually shift from the superficial surface to the deep part of the Si (Figure 3b). Similar phenomenon was also observed in PD2, where the area with high photon-generation rate is found to shift to central part of the Ge when the wavelength is 1550 nm. Figure 3c plots the corresponding photocurrent of the two PDs. It is clear that the photocurrent of PD1 will increase gradually and reach the maximum value at 660 nm. Further an increase in wavelength however will lead to decrease in photocurrent. Such an evolution in photocurrent is different from what is observed in PD2, whose photocurrent keeps increasing in the

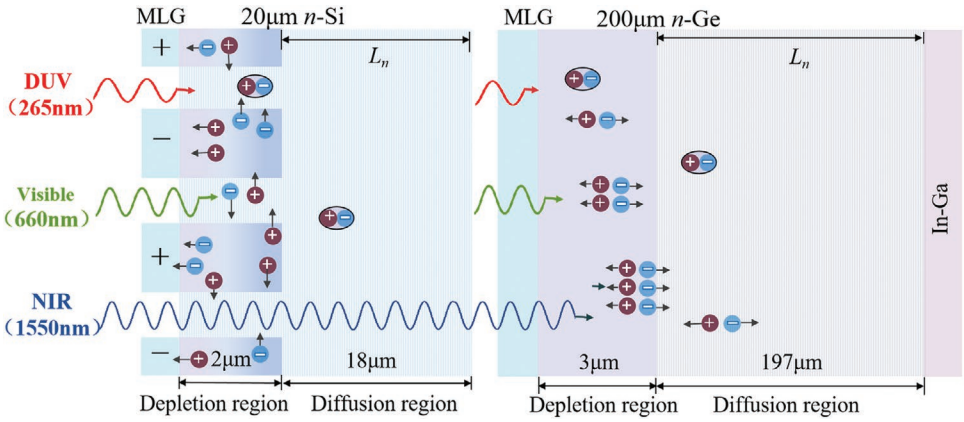

Figure 2. The operation mechanism of wavelength sensor under different light illuminations.

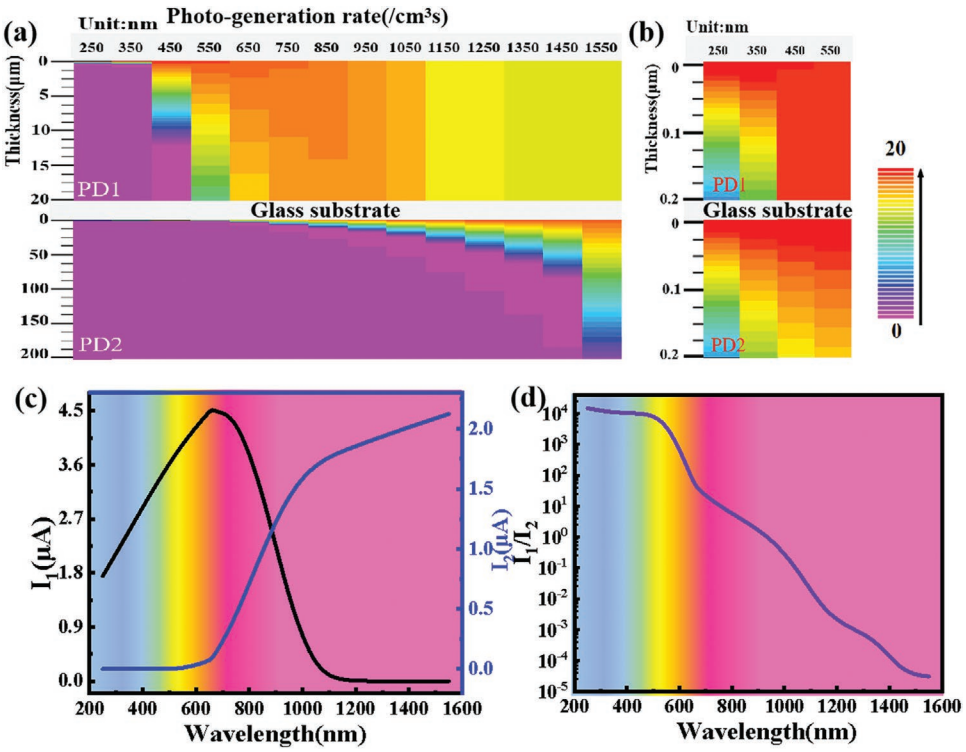

Figure 3. a) Simulated photon-generation rate under different wavelengths of illumination. b) The magnified mapping of the photon-generation rate at the surface of the first and second PD under illumination with wavelength ranging from 250 to 550 nm. c) Simulated photocurrent of the PD1 and PD2 in the whole sensing range. d) The simulated photocurrent ratio of PD1 over PD2.

region from 250 to 1550 nm. Interestingly, careful examination of both photocurrent finds that photocurrent ratio decreases monotonously from 1.45×10^4 to 3.06×10^{-5} as the wavelength increases from 250 to 1550 nm (Figure 3d).

Further experimental analysis reveals that the two heterojunction PDs indeed display completely different spectral response when they were illuminated by different wavelengths of light. **Figure** 4a plots the photoresponse of MLG/thin Si/MLG PD in the range from UV to NIR region. One can see that at a bias voltage of 2 V, the PD1 exhibits obvious photoresponse to various light illumination with peak sensitivity at 660 nm, which is blue-shifted compared with graphene-bulk Si device.[37] This photoresponse is understandable because the weak *p*-type graphene due to the absorption of oxygen molecules can form a typical Schottky junction a barrier height of 0.7 eV. As a result, the photo-generated EHPs at the graphene-Si interface will be separated by the built-in electric field, and form photocurrent in the external circuit, according to the *E*–*K* diagram in Figure 4b and the corresponding density of states in Figure 4c. Obviously, this spectral photoresponse is different from that of MLG/Ge, whose peak sensitivity is at 1550 nm, in consistence with above simulation results. Considering the fact that selection of 2 V is able to separate all of the photo-generated EHPs and further increase in bias voltage will no longer lead to increase in photocurrent,[38] a bias voltage of 2 V was thereby applied on the PD1 in this study. It is worth noting that while a number of silicon PDs without graphene have shown typical cutoff wavelength at 1100 nm,[39–41] however, the present MLG/thin Si/MLG has a photoresponse in the range from 1100 to 1550 nm. We believe this abnormal photoelectric effect is associated with the hot electron emission effect due to the graphene.[42–44] The schematic energy band diagram in Figure S7, Supporting Information, shows the generation mechanism of the hot electron emission: the barrier height of the MLG/Si Schottky junction is estimated to be 0.7 eV. When the Si/MLG is shined by the light illumination with wavelength longer than 1100 nm, the incident photons will be mainly absorbed by the MLG, as opposed to the Si. As a result, when the photon energy is larger than the barrier height, the excited electrons in the MLG will inject into the Si, leading to an obvious photoresponse in the NIR region. Figure 4d shows the evolution of photocurrent ratio in the DUV to NIR region, it is revealed that when the wavelength of incident light increases from 265 to 1550 nm, the photocurrent ratio (I_1/I_2) gradually decreases from 1.21×10^4 to 9.43×10^{-5}, in consistence with the above simulation result. Figure 4e plots the experimental results of the photocurrent ratio as a function of various wavelengths. It is seen that even though the relationship between wavelength and photocurrent ratio is nonlinear in the 265–1550 nm region, it is however possible for us to accurately estimate the incident wavelength as the relationship can be described piecewise using the following Boltzmann fitting (265–660 nm) and Allometric fitting (660–1550 nm):

$$\lambda = \begin{cases} 465.094 + 20.693 \ln\left(\dfrac{9996.649}{\dfrac{I_{Ph_1}}{I_{Ph_2}} - 2033.003} - 1\right), & 265\,\text{nm} \le \lambda \le 660\,\text{nm} \\ \dfrac{1}{e^{-19.772}} \ln \dfrac{\dfrac{I_{Ph_1}}{I_{Ph_2}}}{1.175 \times 10^{59}}, & 660\,\text{nm} < \lambda \le 1550\,\text{nm} \end{cases} \quad (1)$$

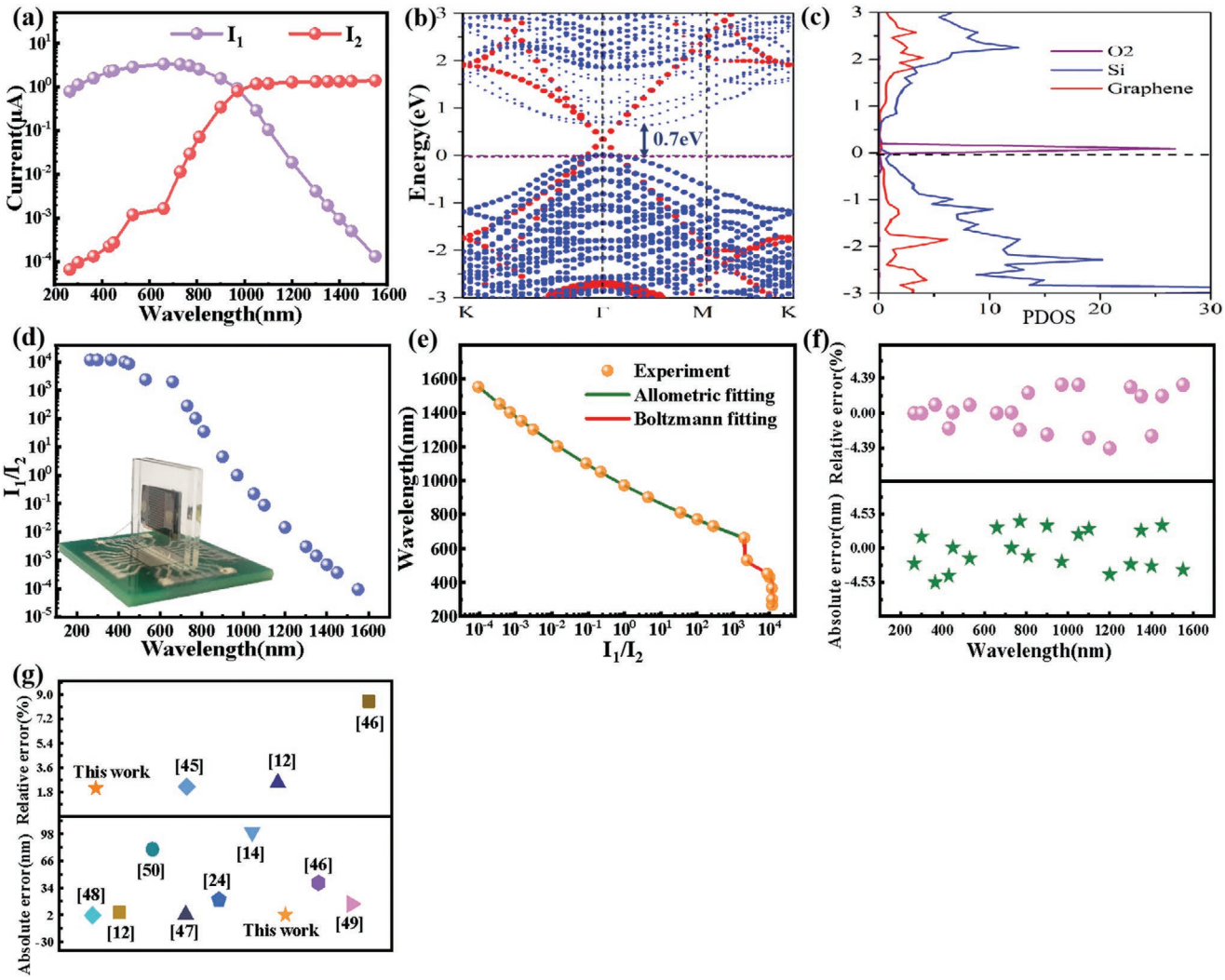

Figure 4. a) The spectral response of PD1 with the bias of 2 V and the PD2 with the bias of 0 V under the light intensity of 1.2 mW cm^{-2}. b) *E–k* diagram of the graphene-Si interface. c) The corresponding density of states. d) Photocurrent ratio at different incident wavelengths, the inset is the physical image of the wavelength sensor. e) Subsection fitting data: the red curve is Boltzmann fitting and green curve is allometric fitting. f) The relative error and absolute error of the wavelength sensor. g) Comparison of both absolute error and relative error between our sensor and other wavelength sensors.

In order to evaluate how and to what extent the above fitting curve can quantitatively determine the wavelength, the relative error was then analyzed using the following formula:

$$\text{Relative error} = \frac{\left(\frac{I_{Ph_1}}{I_{Ph_2}}\right)_{\lambda_e} - \left(\frac{I_{Ph_1}}{I_{Ph_2}}\right)_{\lambda_t}}{\left(\frac{I_{Ph1}}{I_{Ph_2}}\right)_{\lambda_t}} \times 100\% \quad (2)$$

where $\left(\frac{I_{Ph_1}}{I_{Ph_2}}\right)_{\lambda_t}$ is the theoretical photocurrent ratio, $\left(\frac{I_{Ph_1}}{I_{Ph_2}}\right)_{\lambda_e}$ is the experimental photocurrent ratio. Figure 4f summarizes the errors of wavelength sensor from 265 to 1550 nm. It can be seen that under an intensity of 1.2 mW cm^{-2}, the average relative error in the whole sensing range is 2.1%, with a maximum relative error of 4.4% at 1200 nm. What's more, the current device has an average absolute error of 2.3 nm, with the maximum value of –4.6 at 365 nm. Comparison of these two parameters with a previously reported device reveals that the average relative error of our sensor is lower than that of the CFAs sensor (relative error: 2.2%, Figure 4g),[45] filter-less BiCMOS RGB sensor (2.5%), and filter-based microspectrometers (8.5%).[12,46] On the other hand, the absolute error is comparable to the spectral sensors based on photonic crystal slabs (absolute error: 1.5 nm) and a quantum dot spectrometer (2.5 nm),[47,48] but is much better than other sensors including filter-less BiCMOS RGB sensor (absolute error: 5.0 nm),[12] single-nanowire spectrometers (15 nm),[49] multi-wavelength analysis based on CMOS buried Quad *p–n* junction PD (20 nm),[24] filter-based miniature spectrometers (40 nm),[46] in-situ formed gradient bandgap-tunable perovskite PDs (80 nm), and filterless narrowband visible PDs (100 nm).[14,50]

Even though the above result has corroborated that the present wavelength sensor can indeed achieve the precise determination of the incident wavelength. However, there is an undeniable the fact that the quantitative discrimination of the

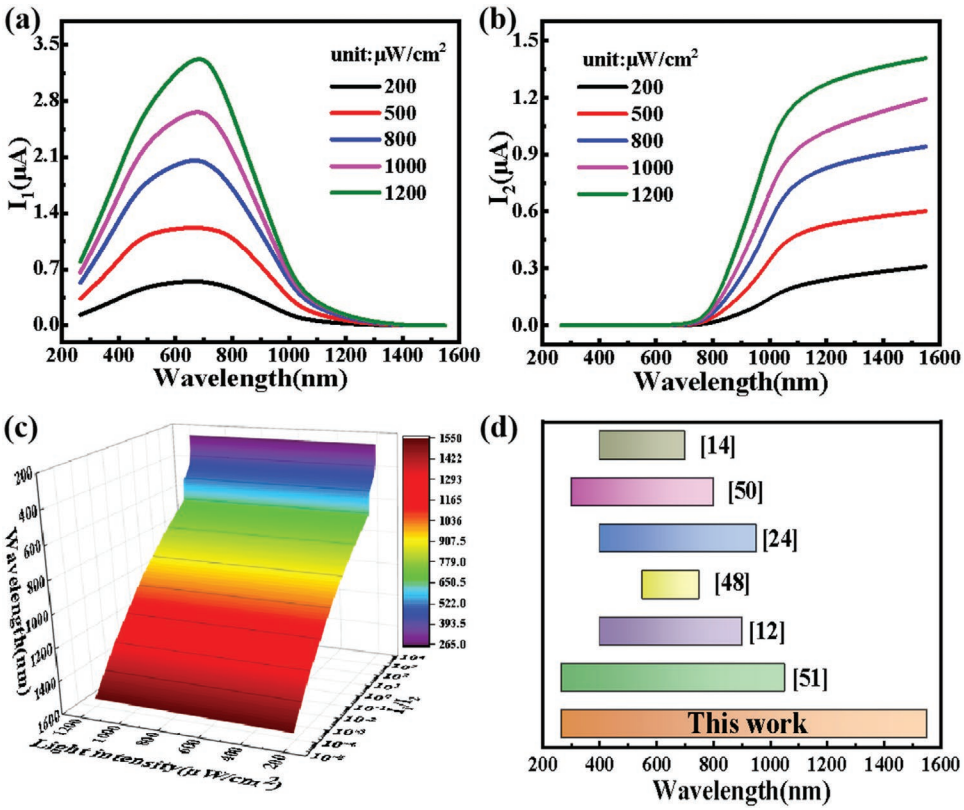

Figure 5. a) Photocurrent of the PD1 under illumination with various intensities at a bias voltage of 2 V. b) Photocurrent of the PD2 under various illuminations with different intensities, at 0 V. c) The relationship between the photocurrent ratio and the wavelength under various light illuminations with different intensities. d) Comparison of sensing range of the present sensor and other devices.

wavelength is subject to the change of light intensity. In order to describe the relationship between the photocurrent ratio and the wavelength in a more comprehensive way, new piecewise fitting functions after considering light intensity can be obtained (see Supporting Information). **Figure 5**a,b shows the evolution of photocurrent of both PDs when the light intensity gradually increases from 0.2 to 1.2 mW cm^{-2}. It is apparent that the photocurrent of both PDs increases due to enhanced photon generation at high intensity. The corresponding relationship between the photocurrent ratio and wavelength according to our calculation is slightly increased, but still follows a typical monotonic function (Figure 5c). Table S1, Supporting Information, shows the sensing errors in three different regions: DUV (265 nm), visible (660 nm), and NIR (1050 nm). It can be seen that in the short and medium wavelength region, as the light intensity gradually increases from 200 to 1200 μW cm^{-2}, our wavelength sensor has a relatively large absolute error (–5.5 to 5.6 nm) but a small relative error (–0.7% to 1.2%). On the contrary, in the longer wavelength (NIR), the average relative error of our wavelength detection device is much larger than that in short wavelength. What is more, our device is also characterized by a broader sensing range. Figure 5d shows the working range of various wavelength sensors. Obviously, compared with other wavelength sensors, our device has a sensing region ranging from DUV to NIR, which is at least two or three times longer than that of other wavelength sensors,[12,14,24,48,50,51] such as two parallel $PtSe_2$/thin Si Schottky junctions (265–1050 nm), filter-less BiCMOS (400–900 nm), and Quad *p–n* junction (400–950 nm). This broad sensing region along with the competitive device performance renders the current wavelength highly promising in some optoelectronic devices and systems.

3. Conclusion

In summary, we have successfully developed a wavelength sensor composed of MLG/thin Si/MLG heterojunction PD and MLG/Ge Schottky junction PD. The proposed wavelength sensor can easily distinguish different wavelengths in the range from DUV to NIR. From TCAD simulation, the photon-generation rate of the two PDs is different under various wavelengths of radiation, leading to completely different spectral responses. The relationship between the photocurrent ratio and the wavelength follows a typical monotonic function, through which the wavelength of the incident light can be determined. Further device analysis finds that wavelength sensor can quantitatively distinguish wavelength of incident monochromatic light in broad range from 265 to 1550 nm, with an average relative error and average absolute error of 2.1% and 2.3 nm, respectively, which are very competitive in comparison with other wavelength sensors previously reported. We believe the present device configuration is also applicable to other semiconductor materials, as long as their absorption coefficient is highly dependent on the light wavelength.

4. Experimental Section

Materials Synthesis and Device Fabrication: In this work, the 20 µm-thick phosphorus doped *n*-type (100) single-crystalline silicon film with resistivity of 1–10 Ω cm (diameter: 2 inches, doping concentration of 10^{16} cm^{-3}, double side polished) was purchased from the University Wafer INC, the 200 µm-thick antimony doped *n*-type (100) single-crystalline germanium wafer with resistivity of 0.1–6 Ω cm (diameter: 4 inches, doping concentration of 10^{16} cm^{-3}, single side polished) was purchased from Beijing Voskey Technology Co., Ltd. In addition, high-quality single layer graphene was grown at 1005 °C by using a mixed gas of CH_4 (1 sccm) and H_2 (50 sccm) via a CVD method in which 50 µm-thick copper foils were employed as the catalytic substrates. The detailed process of growing graphene has been described in our previous work. After growth, the graphene films were spin-coated with 5 wt% polymethylmethacrylate (PMMA) in chlorobenzene, and then the underlying Cu foil were removed in Marble's reagent solution ($CuSO_4$: HCl: H_2O = 10 g: 50 mL: 50 mL). The graphene films were rinsed in deionized water to remove the remaining ions. To assemble the Gr/thin Si/Gr heterojunction device, an *n*-type Si wafer was first cleaned with alcohol and acetone under ultrasonication for 10 min, which was placed on a glass substrate in advance, and then covered with a layer graphene film supported by PMMA. Lithography was used to define the interdigital pattern of graphene, and then an oxygen plasma was used to remove the graphene in the channels. Finally, silver paste was coated on the graphene at the ends of the fingers to form good ohmic contact for device analysis.

To assemble the MLG/Ge Schottky junction device, lithography was first used to define the window pattern of Ge wafer coated with 50 nm-thick alumina, then the Ge wafer was immersed in dilute hydrochloric acid solution for eight hours. The as-treated Ge wafer was soaked in deionized water, and then slowly lifted to mount the graphene film on the Ge. Afterward, the shadow mask method was used to pattern the Au electrode by the thermal evaporation technique. Finally, the silver paste and indium-gallium alloy were coated on the top of the graphene and the bottom of the Ge wafer respectively to form ohmic contact for device analysis. To assemble the color detector, we attached the silicon-based device to the top of the germanium-based device and blocked the light around it to prevent light from coming in from the side.

Material Characterization, Device Analysis, and Simulation: The morphology of graphene cross finger electrode, thin silicon cross section and Ge window were observed using a FESEM instrument (Hitachi, SU8020). The graphene film was studied by a Raman spectrometer (Horiba Jobin Yvon, LabRAM HR800). The absorption spectra of graphene in quartz, the planar Si substrate, and Ge were recorded on a Shimadzu UV-2550 UV–vis spectrophotometer. The photoelectric characteristics were performed on a semiconductor parameter testing system (Keithley 2400), and spectral response was measured on a monochrometer (LE-SP-M300). Prior to device analysis, the power intensity of the incident light was calibrated by a power meter (Thorlabs GmbH., PM 100D). All studies were conducted under ambient conditions at room temperature. Simulation was carried out using Synopsys Sentaurus TCAD to analyze the photon-generation rate and photocurrent in the device.

Supporting Information

Supporting Information is available from the Wiley Online Library or from the author.

Acknowledgements

This work was supported by the National Natural Science Foundation of China (NSFC, Nos. 62074048), the Fundamental Research Funds for the Central Universities (JZ2018HGXC0001, JZ2018HGPB0275, and PA2020GDKC0014), and the Open Foundation of Anhui Provincial Key Laboratory of Advanced Functional Materials and Devices (4500-411104/011).

Conflict of Interest

The authors declare no conflict of interest.

Data Availability Statement

Research data are not shared.

Keywords

average relative error, Boltzmann fitting, photocurrent ratio, photon-generation rate, wavelength sensors

Received: August 19, 2021
Revised: September 21, 2021
Published online: November 2, 2021

[1] J. McDowell, *IEEE Potentials* **2008**, *27*, 34.
[2] S. P. Burgos, S. Yokogawa, H. A. Atwater, *ACS Nano* **2013**, *7*, 10038.
[3] A.-M. Cailean, B. Cagneau, L. Chassagne, M. Dimian, V. Popa, *IEEE Sens. J.* **2015**, *15*, 4632.
[4] J. Meng, J. J. Cadusch, K. B. Crozier, *Nano Lett.* **2020**, *20*, 320.
[5] N. Strobel, N. Droseros, W. Kontges, M. Seiberlich, M. Pietsch, S. Schlisske, F. Lindheimer, R. R. Schroder, U. Lemmer, M. Pfannmoller, N. Banerji, G. Hernandez-Sosa, *Adv. Mater.* **2020**, *32*, e1908258.
[6] L. A. Greenawald, G. R. Boss, J. L. Snyder, A. Reeder, S. Bell, *ACS Sens.* **2017**, *2*, 1458.
[7] K. Engelhardt, P. Seitz, *Appl. Opt.* **1993**, *32*, 3015.
[8] S. Yokogawa, S. P. Burgos, H. A. Atwater, *Nano Lett.* **2012**, *12*, 4349.
[9] H. Park, Y. Dan, K. Seo, Y. J. Yu, P. K. Duane, M. Wober, K. B. Crozier, *Nano Lett.* **2014**, *14*, 1804.
[10] J. H. Han, D. Kim, T.-W. Lee, Y. Jeon, H. S. Lee, K. C. Choi, *ACS Photonics* **2018**, *5*, 3322.
[11] K. Liang, C. W. Chow, Y. Liu, *Opt. Express* **2016**, *24*, 9383.
[12] A. Polzer, W. Gaberl, H. Zimmermann, *Electron. Lett.* **2011**, *47*, 10.
[13] A. Armin, R. D. Jansen-van Vuuren, N. Kopidakis, P. L. Burn, P. Meredith, *Nat. Commun.* **2015**, *6*, 6343.
[14] Q. Lin, A. Armin, P. L. Burn, P. Meredith, *Nat. Photonics* **2015**, *9*, 687.
[15] Y. Higashi, K.-S. Kim, H.-G. Jeon, M. Ichikawa, *J. Appl. Phys.* **2010**, *108*, 034502.
[16] V. Gautam, M. Bag, K. S. Narayan, *J. Am. Chem. Soc.* **2011**, *133*, 17942.
[17] K. H. Lee, D. S. Leem, J. S. Castrucci, K. B. Park, X. Bulliard, K. S. Kim, Y. W. Jin, S. Lee, T. P. Bender, S. Y. Park, *ACS Appl. Mater. Interfaces* **2013**, *5*, 13089.
[18] S. Nishiwaki, T. Nakamura, M. Hiramoto, T. Fujii, M.-a. Suzuki, *Nat. Photonics* **2013**, *7*, 240.
[19] I. K. Kim, X. Li, M. Ullah, P. E. Shaw, R. Wawrzinek, E. B. Namdas, S. C. Lo, *Adv. Mater.* **2015**, *27*, 6390.
[20] W. Wang, F. Zhang, M. Du, L. Li, M. Zhang, K. Wang, Y. Wang, B. Hu, Y. Fang, J. Huang, *Nano Lett.* **2017**, *17*, 1995.
[21] L. Z. Qiu, S. Y. Wei, H. S. Xu, Z. X. Zhang, Z. Y. Guo, X. G. Chen, S. Y. Liu, D. Wu, L. B. Luo, *Nano Lett.* **2020**, *20*, 644.

[22] B. C. Zhang, Y. H. Shi, J. Mao, S. Y. Huang, Z. B. Shao, C. J. Zheng, J. S. Jie, X. H. Zhang, *Adv. Mater.* **2021**, *33*, 2008171.
[23] A. Ali, K. Shehzad, H. W. Guo, Z. Wang, P. Wang, A. Qadir, W. D. Hu, T. L. Ren, B. Yu, Y. Xu, presented at *63rd IEEE Annual Int. Electron Devices Meeting (IEDM)*, xxxx, San Francisco December **2017**.
[24] C. Richard, T. Courcier, P. Pittet, S. Martel, L. Ouellet, G. N. Lu, V. Aimez, P. G. Charette, *Opt. Express* **2012**, *20*, 2053.
[25] A. Reina, X. T. Jia, J. Ho, D. Nezich, H. B. Son, V. Bulovic, M. S. Dresselhaus, J. Kong, *Nano Lett.* **2009**, *9*, 30.
[26] C. Xie, P. Lv, B. Nie, J. Jie, X. Zhang, Z. Wang, P. Jiang, Z. Hu, L. Luo, Z. Zhu, L. Wang, C. Wu, *Appl. Phys. Lett.* **2011**, *99*, 133113.
[27] G. H. Han, F. Güneş, J. J. Bae, E. S. Kim, S. J. Chae, H.-J. Shin, J.-Y. Choi, D. Pribat, Y. H. Lee, *Nano Lett.* **2011**, *11*, 4144.
[28] J. M. Dawlaty, S. Shivaraman, J. Strait, P. George, M. Chandrashekhar, F. Rana, M. G. Spencer, D. Veksler, Y. Chen, *Appl. Phys. Lett.* **2008**, *93*, 131905.
[29] R. R. Nair, P. Blake, A. N. Grigorenko, K. S. Novoselov, T. J. Booth, T. Stauber, N. M. R. Peres, A. K. Geim, *Science* **2008**, *320*, 1308.
[30] Y. Zhao, J. Zhang, D. Jiang, C. Shan, Z. Zhang, B. Yao, D. Zhao, D. Shen, *ACS Appl. Mater. Interfaces* **2009**, *1*, 2428.
[31] Y. Cai, S. Shen, C. Zhu, X. Zhao, J. Bai, T. Wang, *ACS Appl. Mater. Interfaces* **2020**, *12*, 25031.
[32] L. H. Zeng, M. Z. Wang, H. Hu, B. Nie, Y. Q. Yu, C. Y. Wu, L. Wang, J. G. Hu, C. Xie, F. X. Liang, L. B. Luo, *ACS Appl. Mater. Interfaces* **2013**, *5*, 9362.
[33] L. Wang, H. H. Luo, H. H. Zuo, J. Q. Tao, Y. Q. Yu, X. P. Yang, M. L. Wang, J. G. Hu, C. Xie, D. Wu, L. B. Luo, *IEEE Trans. Electron Devices* **2020**, *67*, 3211.
[34] L. Wang, J.-J. Li, Q. Fan, Z.-F. Huang, Y.-C. Lu, C. Xie, C.-Y. Wu, L.-B. Luo, *J. Mater. Chem. C* **2019**, *7*, 5019.
[35] A. Falco, R. Nagel, P. Lugli, E. Bezzeccheri, R. Liguori, A. Rubino, presented at *15th IEEE Sensors Conf*, xxxx, Orlando November **2016**.
[36] M. Arsalan, J. Liu, A. Zaslavsky, S. Cristoloveanu, J. Wan, *IEEE Trans. Electron Devices* **2020**, *67*, 3256.
[37] P. Lv, X. J. Zhang, X. W. Zhang, W. Deng, J. S. Jie, *IEEE Electron Device Lett.* **2013**, *34*, 1337.
[38] L.-B. Luo, T. Fang, C. Xie, L. Wang, D. Wu, F.-X. Liang, *J. Mater. Chem. C* **2021**, *9*, 8855.
[39] E. Mulazimoglu, S. Coskun, M. Gunoven, B. Butun, E. Ozbay, R. Turan, H. E. Unalan, *Appl. Phys. Lett.* **2013**, *103*, 083114.
[40] L. Wang, J. Jie, Z. Shao, Q. Zhang, X. Zhang, Y. Wang, Z. Sun, S.-T. Lee, *Adv. Funct. Mater.* **2015**, *25*, 2910.
[41] C.-Y. Wu, J.-W. Kang, B. Wang, H.-N. Zhu, Z.-J. Li, S.-R. Chen, L. Wang, W.-H. Yang, C. Xie, L.-B. Luo, *J. Mater. Chem. C* **2019**, *7*, 11532.
[42] J. P. Mailoa, A. J. Akey, C. B. Simmons, D. Hutchinson, J. Mathews, J. T. Sullivan, D. Recht, M. T. Winkler, J. S. Williams, J. M. Warrender, P. D. Persans, M. J. Aziz, T. Buonassisi, *Nat. Commun.* **2014**, *5*, 3011.
[43] M. L. Brongersma, N. J. Halas, P. Nordlander, *Nat. Nanotechnol.* **2015**, *10*, 25.
[44] M. Casalino, *IEEE J. Quantum Electron.* **2016**, *52*, 4000110.
[45] B. K. Gunturk, J. Glotzbach, Y. Altunbasak, R. W. Schafer, R. M. Mersereau, *IEEE Signal Process. Mag.* **2005**, *22*, 44.
[46] U. Kurokawa, B. I. Choi, C.-C. Chang, *IEEE Sens. J.* **2011**, *11*, 1556.
[47] J. Bao, M. G. Bawendi, *Nature* **2015**, *523*, 67.
[48] Z. Wang, S. Yi, A. Chen, M. Zhou, T. S. Luk, A. James, J. Nogan, W. Ross, G. Joe, A. Shahsafi, K. X. Wang, M. A. Kats, Z. Yu, *Nat. Commun.* **2019**, *10*, 1020.
[49] Z. Y. Yang, T. Albrow-Owen, H. X. Cui, J. Alexander-Webber, F. X. Gu, X. M. Wang, T. C. Wu, M. H. Zhuge, C. Williams, P. Wang, A. V. Zayats, W. W. Cai, L. Dais, S. Hofmann, M. Overend, L. M. Tong, Q. Yang, Z. P. Sun, T. Hasan, *Science* **2019**, *365*, 1017.
[50] H. Sun, W. Tian, X. Wang, K. Deng, J. Xiong, L. Li, *Adv. Mater.* **2020**, *32*, 1908108.
[51] W. H. Yang, X. Y. Jiang, Y. T. Xiao, C. Fu, J. K. Wan, X. Yin, X. W. Tong, D. Wu, L. M. Chen, L. B. Luo, *Mater. Horiz.* **2021**, *8*, 1976.